

Tailoring *c*-Axis Orientation in Epitaxial Ruddlesden–Popper $\text{Pr}_{0.5}\text{Ca}_{1.5}\text{MnO}_4$ Films

Sarah Hoffmann-Urlaub,* Ulrich Ross, Jörg Hoffmann, Alexandr Belenchuk, Oleg Shapoval, Vladimir Roddatis, Qian Ma, Birte Kressdorf, Vasily Moshnyaga, and Christian Jooss

Interest in layered Ruddlesden–Popper (RP) strongly correlated manganites of $\text{Pr}_{0.5}\text{Ca}_{1.5}\text{MnO}_4$ as well as in their thin film polymorphs is motivated by the high temperature of charge orbital ordering above room temperature. The *c*-axis orientation in epitaxial films is tailored by different SrTiO_3 (STO) substrate orientations and CaMnO_3 (CMO) buffer layers. Films on STO(110) show in-plane alignment of the *c*-axis parallel to the [100] direction. On STO(100), two possible directions of the in-plane *c*-axis lead to a mosaic like, quasi 2D nanostructure, consisting of RP, rock-salt, and perovskite blocks. With the CMO buffer layer, $\text{Pr}_{0.5}\text{Ca}_{1.5}\text{MnO}_4$ epitaxial films with *c*-axis out-of-plane are realized. Different physical vapor deposition techniques as ion beam sputtering, pulsed laser deposition and metalorganic aerosol deposition are applied in order to distinguish effects of growth conditions from intrinsic epitaxial properties. Despite their very different growth conditions, surface morphology, crystal structure, and orientation of the thin films reveal a high level of similarity as verified by X-ray diffraction, scanning, and high resolution transmission electron microscopy. For different epitaxial relations stress in the films is relaxed by means of modified interface chemistry. The charge ordering in the films occurs at a temperature close to that expected in bulk material.

1. Introduction

Charge ordered 3D perovskite manganites such as $\text{Pr}_{1-x}\text{Ca}_x\text{MnO}_3$ (PCMO) have been investigated intensively due to their unique electrical and magnetic properties, for example, colossal magneto^[1] and electroresistance,^[2,3] photoinduced phase transitions,^[4,5] and thermoelectricity.^[6] Recently, layered Ruddlesden–Popper (RP) perovskites have attracted considerable attention as they display novel physical properties directly related to their 2D structure, such as high activity and stability during oxygen evolution reaction^[7] and a charge ordering temperature above room temperature,^[8] making them a model system for energy and catalytic applications.

The RP-phases are described by the general formula $\text{A}_{n+1}\text{B}_n\text{X}_{3n+1}$, where *n* is the order of the RP-phase denoting the number of 2D perovskite layers that are enclosed by rock-salt (A–O) layers along the stacking direction. The *n* = ∞ corresponds to the 3D perovskite, for example, PCMO. In contrast to bulk perovskites,


epitaxial thin films can offer modified microstructure related properties due to growth-induced defects and lattice misfit strain due to the substrate. The film microstructure can thus be tailored by growth on substrates with different orientations^[9,10] and changing lattice constants.^[11] In general, the properties of transition metal oxides depend strongly on point defects such as oxygen vacancies,^[12,13] which in turn are related to the preparation method. Moreover, electronic and magnetic ordering on the nanoscale are affected by lattice distortions^[14,15] mediated by cooperative tilting and rotation of the MnO_6 octahedra, which yields a change of charge carrier mobility^[16] and electrical resistance^[17] as well as the charge ordering temperature.^[18]

Epitaxial thin films based on nickelates ($\text{La}_{n+1}\text{Ni}_n\text{O}_{3n+1}$),^[19,20] titanates ($\text{Sr}_{n+1}\text{Ti}_n\text{O}_{3n+1}$),^[21–24] strontium oxides ($\text{La}_{n+1}\text{Sr}_n\text{O}_{3n+1}$),^[25,26] and manganites ($\text{La}_{n-nx}\text{Ca}_{1+nx}\text{Mn}_n\text{O}_{3n+1}$)^[27] or ($\text{La}_2\text{Sr}_2\text{Mn}_3\text{O}_{10}$)^[26] have been grown by co-deposition up to *n* = 3. The limited thermodynamic stability of RP phases with *n* ≥ 4 requires an “atomic-layer-epitaxy” growth mode^[28,29] with sequential deposition of the perovskite and rock-salt monolayers therefore creating an enforced generation of a stacking sequence along [001]-direction.

Dr. S. Hoffmann-Urlaub, Dr. U. Ross, Dr. J. Hoffmann, Dr. V. Roddatis, Q. Ma, B. Kressdorf, Prof. Dr. C. Jooss
 Georg-August University of Göttingen
 Institute for Materials Physics
 Friedrich-Hund Platz 1, 37077 Göttingen, Germany
 E-mail: shoffma3@gwdg.de

Dr. A. Belenchuk, Dr. O. Shapoval
 Institute of Electronic Engineering and Nanotechnologies
 Academiei str., 3/3, Chisinau MD-2028, Republic of Moldova

Prof. Dr. V. Moshnyaga
 Georg-August University of Göttingen
 I. Institute of Physics
 Friedrich-Hund Platz 1, 37077 Göttingen, Germany

 The ORCID identification number(s) for the author(s) of this article can be found under <https://doi.org/10.1002/admi.202002049>.

© 2021 The Authors. Advanced Materials Interfaces published by Wiley-VCH GmbH. This is an open access article under the terms of the Creative Commons Attribution-NonCommercial-NoDerivs License, which permits use and distribution in any medium, provided the original work is properly cited, the use is non-commercial and no modifications or adaptations are made.

DOI: 10.1002/admi.202002049

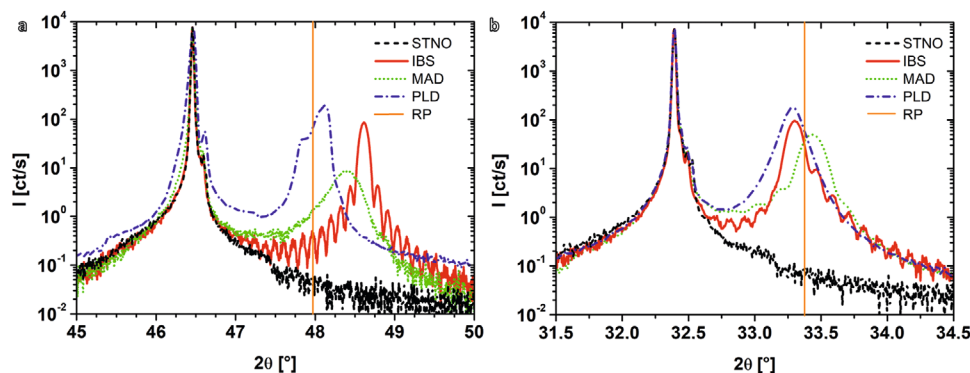


Figure 1. XRD patterns of thin films grown by different techniques on: a) STNO(001) substrates with a detailed view on the (220) reflection of the films and b) on STNO(110) substrates with an enlarged view on the (020) reflection of the film. The black curves show the scans of the bare substrates and the orange lines represent the nominal RP peak positions. All intensities are normalized to the substrate peak.

Here we are focusing on thin films of A-site half-doped first order ($n = 1$) system $\text{Pr}_{0.5}\text{Ca}_{1.5}\text{MnO}_4$ (RP-PCMO) prepared by physical vapor technique based co-deposition. Experiments solely on RP-PCMO nanoparticles have been reported so far.^[30] However, energy conversion and storage applications often require the availability of the RP material as thin films, where thin film epitaxy is highly desirable for the preparation of well-defined junctions. Considering the desire for photovoltaic thin film applications (e.g., ref. [31]) with electrically conducting Nb-doped SrTiO_3 substrates, we focus here on the growth on STO substrates with (001) and (110) orientations in order to access multiple strain states in RP-PCMO/STO films. In addition, we have studied the growth of RP-PCMO on a CaMnO_3 (CMO) buffer layer so as to release the lattice misfit strain. To distinguish between the preparation- and substrate-related effects in view of their impact on the growth mechanisms and characteristics, the films were grown by means of fundamentally different deposition techniques, that is, ion beam sputtering (IBS), pulsed laser deposition (PLD) and metalorganic aerosol deposition (MAD).

2. Results and Discussion

For each deposition method, a suitable parameter set was identified to grow phase pure, homogeneous and smooth thin films in the desired stoichiometry and crystal structure (see Figure S1 (Supporting Information)). Thus, on the same type of substrate very similar results are obtained for all three methods with respect to the film morphology (see Figure S2 (Supporting Information)) and structure. Hence, not all results from samples grown by all used techniques are shown, but only the most-suited films are presented.

The lattice constant of the cubic STO substrate is $a_{\text{STO}} = 3.906 \text{ \AA}$, while for the RP phase in the space group $Fmm2$ the values of $a_{\text{RP}} = 5.365 \text{ \AA}$, $b_{\text{RP}} = 5.354 \text{ \AA}$ and $c_{\text{RP}} = 11.840 \text{ \AA}$ are found in bulk materials.^[7,32] This implies that there are no lowest common multiples for any combinations of axes that would enable a reasonably good matching of both materials to enable a commensurate epitaxy. Between the c -axis of the RP phase ($c_{\text{RP}} = 11.840 \text{ \AA}$) and tripled length of the $a_{\text{STO}} = 3.906 \text{ \AA}$ a lattice mismatch of only 1% would be expected, whereas along the a - and b - directions the lattice mismatch between the RP-PCMO

film and STO substrate is significantly larger. Parallel to [010]/[001] of the substrate the mismatch is $\geq 30\%$ and 3% parallel to [110], hence the growth of a completely epitaxial film is unfavorable and the growth of small grains/domains is expected.

Next, we consider the film growth on STNO(110), since in this case a more suitable substrate lattice parameter of 5.525 \AA is provided in one direction. The anisotropic surface structure supports a preferred growth direction of the film. Due to the asymmetry of the substrates lattice parameters, an in-plane growth of the c -axis is expected. The mismatch of the a - or b -axis of the RP-phase parallel to the [110]-direction of the substrate is -3% and 1% for the c -axis parallel to the [001]-direction (compare Figure S3b (Supporting Information)). Due to the evenly matched lattice parameters of the a - and b -axis, the formation of both [100] and [010] crystallites/domains is equiprobable.

For both cases the crystal structure and orientation of the films are examined by means of XRD (see Figure 1). Note that, as the RP [100] and [010] directions cannot be distinguished, only one of them is indexed for reasons of clarity, while for the reference the quadratic mean is used.

As shown by the XRD patterns in Figure 1, the peak positions of the IBS and MAD films grown in (220) orientation noticeably differ from the nominal RP bulk value of 47.97° , whereas in (010)-orientation all peaks are in good agreement with the expected value of 33.376° (see Table 1), indicating less strained films. For the (220) orientation only tensile stress (negative strain values) is observed for all deposition techniques, while the variations in the absolute strain values are most likely originating from the differences in the film thicknesses and the deposition temperatures. In contrast, the strain (if any) in the

Table 1. Analysis of the X-ray scans in Figure 1 for the RP-PCMO films on STNO (100) (left column) and STNO (110) (right column). For the calculation of the strain $\varepsilon = \frac{d-d_0}{d_0}$ is used, where d_0 is the nominal lattice parameter and d of the film.

Deposition Technique	Position (220) reflex [°]	Strain [%]	Position (020) reflex [°]	Strain [%]
PLD	48.14	-0.32	33.28	0.27
IBS	48.61	-1.24	33.30	0.22
MAD	48.39	-0.82	33.43	-0.16

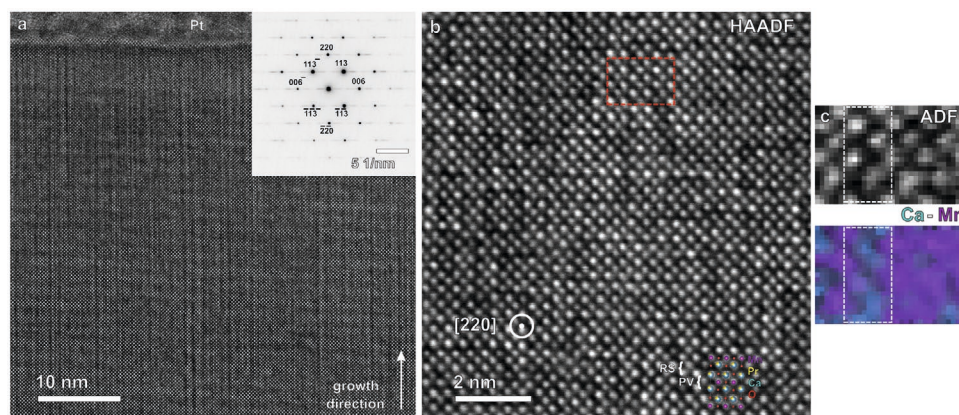


Figure 2. IBS thin film grown on STO(001). a) HRTEM cross-section of the film, capped by a Pt protection layer. Inset: Area-averaged nanodiffraction. b) HAADF-STEM plane view of the film shown in (a) with drawn in positions of the atomic columns, forming a RP-unit cell. c) Top: ADF-STEM image of the region marked in (b), below: STEM-EELS map of Ca-Mn. The white dashed boxes mark the position of the rock-salt layer.

(020) grown films is flipped to compressive for IBS and PLD, while the absolute values are reduced compared to the previous growth direction.

The observed crack microstructure (see Figure S2a (Supporting Information)) appears to be responsible for the release of the in-plane tensile stress. Despite the partial reduction of this strain via crack formation and the presence of other stress relaxation channels such as point or planar defects, the films still possess a large out-of-plane strain. Although the nominal mismatch of the RP-phase to the lattice is the same, the films on STNO(110) with much smaller out-of-plane stress and compressive strain of the order of 0.2–0.3% are consequently crack-free. The out-of-plane strain values for all films and both substrate orientations are listed in Table 1.

Furthermore, the occurrence of Laue fringes, most pronounced for the IBS and MAD films, is an indication for the uniformity of the lattice parameter and, hence, imply that these films are homogeneously strained. Estimated from the distance of the fringes (e.g., ref. [33]) the size of the crystalline domains is 12–15 nm for 35–100 nm thick films in both orientations. This value denotes the lower limit of the size of coherently oriented but slightly tilted or twisted crystal domains.

To understand the interplay of crystal orientation, strain and domain and/or crack formation on an atomic scale level we use high-resolution (scanning) transmission electron microscopy HR(S)TEM to analyze the microstructure of RP-PCMO films grown on both substrate orientations.

In Figure 2a we show a cross-section HRTEM image of a film on STO(001) cut parallel to the [001] direction of the substrate. The diffraction information in the inset confirms the XRD results of (220) out-of-plane orientation (see Figure 1a) and shows that the *c*-axis [001] of the RP film lies in-plane. However, an irregular layering is observed perpendicular to the growth direction. Hence, streaks occur in the diffraction pattern as a result of continuous variations of the lattice plane distances. To understand this in more detail, a planar view on the structure was examined using a high-angle annular dark field (HAADF) STEM as shown in Figure 2b. The in-plane nanostructure is characterized by the arrangement of the two constituent structural units, that is, perovskite (PV, Mn-rich) and rock-salt (RS, CaO) layers, respectively, which can be identified from the ADF image and electron energy

loss spectroscopy (EELS) mapping in Figure 2c. The nanostructure consists of a mosaic-like RP domain pattern with two different orientations of the RP *c*-axis, where individual domains of uniform RP stacking/RP *c*-axis orientation can extend over up to five unit cells. However, it is observed that stacking faults locally form perovskite blocks extended over multiple unit cells. In this configuration the direction of the twofold degenerated *c*-axes is alignment in parallel to either the [100] or the [010] axis of the substrate. The 90° changes in *c*-orientation are forming a network of rock-salt layers throughout large parts of the film (see Figure 2a). As described above, the in-plane strain on the RP-unit cell caused by lattice mismatch is anisotropic; compressive along the *c*-axis and tensile in the perpendicular directions (compare Figure S3 (Supporting Information)). Hence, the formation of a mosaic pattern with alternating alignment of the *c*-axis prevents the buildup of large crystalline domains and thus reduces the misfit strain. As we did not find any sign of phase intermixing/segregation (this is a common way to relax the stress in this materials system^[34]) throughout the whole thickness of the film, it can be denoted as a homogeneous mosaic-type RP phase. The observation of this type of quite uniform network of RP layers leads to the conclusion that this ordered structure grows by means of self-organization with preservation of the mean stoichiometry on the one hand and accommodation of in-plane (biaxial) misfit stress on the other hand.

To investigate the mosaic-like arrangement of the structural units in more detail, we show in Figure 3 HRSTEM imaging (a) complemented by spectroscopy (b) to assign the different chemical species on the A-site (Pr/Ca) and B-site (Mn) to their local positions in the crystal structure (c).

After identifying the two structural units of rock-salt and perovskite it is apparent that the rock-salt layer network is interrupted by partial dislocations.

It is notable that the (incomplete) unit cells are spatially separated and that for two closely spaced cells a 90°-rotated orientation is preferred. Both topological aspects directly correlate with the lattice mismatch between film and substrate, since the strain on two isolated cells is smaller compared to that of two merged cells that would span over a twice as large substrate area. In addition, the alternating arrangement prevents the accumulation of compressive or tensile stress in one direction.

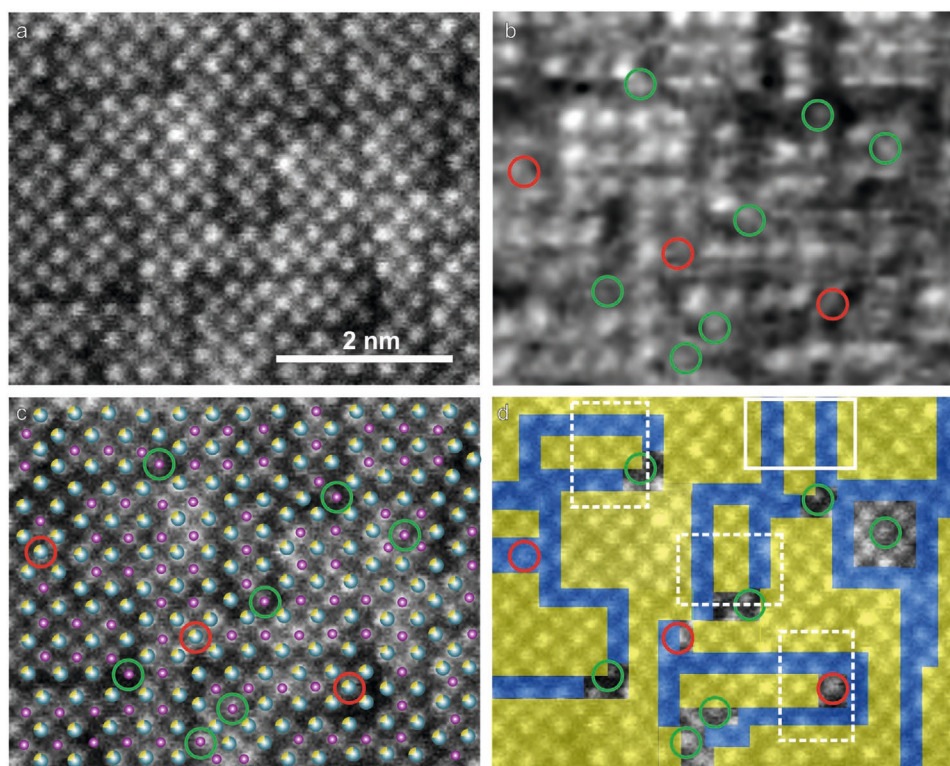


Figure 3. Analysis of nanoscopic mosaic type ordering of the two structural units (rock-salt and perovskite) in a RP-PCMO film grown on STO(001). All images show the same area. a) STEM-ADF image. b) EELS map of the Mn L-edge at 640 eV. In a qualitative manner, green circles mark Mn placed on Pr or Ca sites, while red circles mark the opposite situation of Pr or Ca placed on Mn sites. c) STEM-ADF image with atomic species drawn in, based upon the correlation of (a) and (b). Mn atoms are drawn in purple and Pr/Ca in green and yellow. d) Topology of rock-salt layers (blue) and perovskite blocks (yellow). The white boxes mark the positions of RP-units, dashed lines circumvent incomplete cells and the solid line a complete unit cell.

The corresponding films show a network of cracks (see Figure S2a (Supporting Information)), aligned rectangular with respect to each other as well as to the $\langle 100 \rangle$ -directions of the STO crystal. This microscopic effect can be directly understood from the nanoscale arrangement of the two structural units. As a matter of principle, the bond length across a rock-salt layer is larger compared to that of the perovskite layer.^[35] We assume that the rock-salt bonding is weaker, as it is well known from their tendency to accept interstitial oxygen.^[36] Due to this, it is most probable that the cracks run along the rock-salt layers. Cracks that are even extended into the substrate are an indication of a strong adhesion between substrate and film as it was documented for this materials system earlier.^[37]

The defect and domain structure on STNO(110) substrates is quite different, hence the RP-PCMO growth is investigated by TEM analysis to gain information about ordering of structural units on a substrate with anisotropic surface lattice.

The PCMO-RP films in Figure 4a deposited on (110) oriented substrates show a high degree of ordering. The domains of RP phase are separated by stacking faults and possibly by grain boundaries with very small angles of less than 1° . They reveal spatial extensions of about 20 nm, which is in good agreement to the coherence length of 10–15 nm estimated by XRD analysis. In the planar view the alternate layering of perovskite and rock-salt layers is verified by EELS mapping revealing a stacking sequence of Ca-O rich as well as Mn-O rich layers (b,c).

As a fundamental result films on STNO(110) are crack-free (see Figure S2b (Supporting Information)) and just as smooth as the films on (001) (d). The AFM analysis supports the findings in the SEM images, since the RMSE roughness accounts for 0.2 nm, which is equal to the difference between two SrO/TiO₂ terrace steps of the unterminated substrate.

A different degree of strain in the mosaic RP phase in films on STO (100) and the *c*-axis in-plane RP phase in films on STNO (110) is also supported by the results of X-ray diffraction. As revealed in Table 1, the out-of-plane *a* and *b* lattice parameter in the film with *c*-axis in-plane differ less from the nominal value than the strains in the (110) planes of the mosaic type film. The occurrence of the second peak for the film prepared by PLD in Figure 1a may be an indication for a degenerated lattice parameter that may be attributed to the steric configuration of the RP unit cells in the mosaic pattern, while coherently only one peak is observed for the layered RP structure in the films on STNO (110).

In Figure 5a we present the XRD pattern of a RP-PCMO film grown on a STO(001) substrate buffered by a 10 nm thick CaMnO₃ (CMO) layer. The out-of-plane orientation of the *c*-axis is favored by introducing an [001] oriented orthorhombic CMO buffer layer^[38] with a pseudo-cubic lattice parameter of $d_{\text{CMO}} = 3.72 \text{ \AA}$ that is close to that of the RP-phase $d_{\text{RP}} = 3.79 \text{ \AA}$. We assume that due to the notably reduced in-plane misfit stress of 1.7% between RP-phase and buffer layer as well as the structural similarity of the lattice types an epitaxial growth is

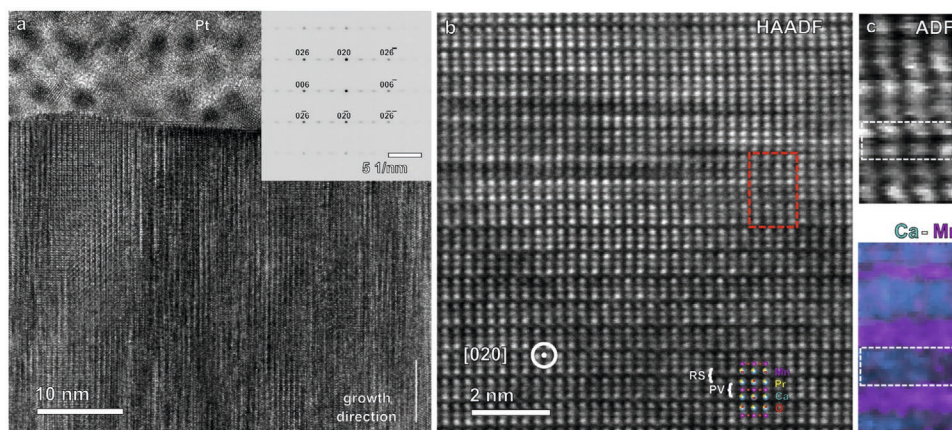


Figure 4. IBS-grown thin film on a STNO(110) substrate. a) HRTEM cross-section of the film, capped by a Pt-layer. Inset: Area-averaged nanodiffraction. b) HAADF-STEM plane view of the film in (a) with drawn in positions of the atoms, forming a RP-unit cell. c) Top: ADF-STEM image of the region marked in (b), below: STEM-EELS map of Ca-Mn. The white dashed boxes mark the position of the rock-salt layer.

enabled. However, the [001] RP-PCMO growth was up to now only detected for MAD-grown films at an elevated growth temperature of 945 °C. The length of the RP *c*-axis extracted from the XRD scans is 11.87 Å, which is in good agreement to the values given above. The size of domains of pure RP-phase was found to be up to a few tens of nanometers. They are separated by anti-phase boundaries induced by stacking faults at the interface to the CMO buffer layer (Figure 5b) that reveals a surface roughness smaller than one RP unit cell.

On basis of the accomplished growth of phase pure RP thin films, the charge order transition temperature is determined by measuring the in-plane resistivity as a function of temperature. This is exemplary depicted for the *c*-axis oriented MAD film (Figure 5c). According to experimental data on bulk RP-PCMO the charge orbital ordering occurs at $T_{CO} \approx 320$ K (for instance^[39,40]). For RP-PCMO films studied on STO(110) and on STO (100) with a CMO buffer, a charge orbital ordering was also observed above room temperature as evidenced by the change of the slope in the resistivity curve in the Arrhenius representation and by the normalized deviation of the measured resistivity *R* from the linear fit of the high temperature region R_{HT} of the Arrhenius plot. As a result the estimated value of 307 K is found to be in excellent agreement with data on bulk RP-PCMO.

3. Conclusion

In summary, epitaxial $\text{Pr}_{0.5}\text{Ca}_{1.5}\text{MnO}_4$ thin films grown by means of ion beam sputtering, pulsed laser and metalorganic aerosol deposition reveal similar properties in terms of surface morphology, crystal orientation, internal structure, strain states, and defect density and types. Hence, no systematic impact of the deposition method on the growth characteristics was readily apparent. This study clearly confirms that by controlling the surface crystal symmetry or rather the lattice parameter of the underlying substrate the structural orientation and strain state of the RP-PCMO thin film grown on top can be adjusted. In detail, on STO(001) growth of the RP-phase in [110] direction is observed, while the in-plane direction of the *c*-axis is degenerated leading to a mosaic like pattern of structural domains in the RP sub-unit cell range. Here, due to the mismatch to the cubic substrate lattice and the related tensile strain, a crack network aligned with respect to the underlying substrate is formed. On the STNO(110) substrate that exhibits an anisotropic surface lattice, the *c*-axis of the unit cells is arranged in parallel to the surface [100] direction. The films with an out-of-plane [020]/[200] orientation and are less strained and crack-free. To induce an out-of-plane *c*-axis orientation in MAD,

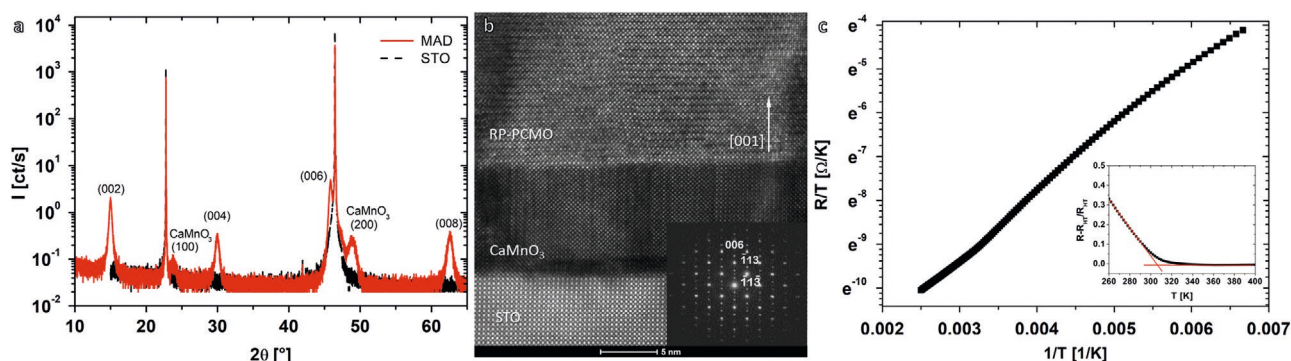


Figure 5. MAD epitaxial RP-PCMO thin film grown on STO(100) with a CaMnO_3 buffer layer. a) Indexed X-ray diffractogram. b) TEM cross-section with the corresponding electron diffraction pattern in the inset. c) In-plane temperature dependent resistivity measurement in Arrhenius representation. Inset: Normalized deviation of the measured resistivity *R* from the linear fit of the high temperature region R_{HT} of the Arrhenius plot.

a CaMnO₃ buffer layer was introduced. From the temperature dependent electrical resistance of RP-PCMO films, compelling evidence for a charge ordering temperature of $T_{CO} = 307$ K was obtained, which is in excellent agreement with the bulk value of RP-PCMO.

4. Experimental Section

Dense ceramic targets of Pr_{0.5}Ca_{1.5}MnO₄ were prepared for PLD and IBS using standard ceramic synthesis methods. Appropriate ratios of Pr₆O₁₁ (CAS 12037-29-5), CaCO₃ (CAS 471-34-1) and Mn₂O₃ (CAS 1317-34-6) powders (Sigma-Aldrich) were mixed and intimately ground using a planetary ball mill (Retsch). The powder was annealed twice for 12 h at 900 °C and once for 12 h at 1100 °C (Nabertherm, HTCT 01/16), with intermediate grindings. Pellets having a diameter of 2.5 cm were uniaxially cold pressed (Janssen HWP 20) at a pressure of 120 bar for 20 min and sintered for 24 h at 1500 °C. In between the process steps the homogeneity and phase purity of the powders and the final target is monitored by XRD.

For the MAD preparation the acetylacetonates of Pr, Ca, and Mn were used as precursors. The solution in organic solvent dimethylformamide (DMFA) (Sigma, Aldrich) was prepared with experimentally determined (Pr + Ca)/Mn and Pr/Ca precursor ratios and concentration of 0.02 mole (calculated for Mn-precursor). Polished substrates of strontium titanate (STO) and the 0.5 wt% doped Nb:SrTiO₃ (STNO) in (100) and (110) orientation were used (CrysTec).

Deposition Techniques: PLD^[41] used a KrF excimer laser (COMPex 205F, Coherent) with a wavelength of 248 nm, a pulse duration of 30 ns and a repetition rate of 5 Hz to fabricate thin films. The oxygen background pressure in the vacuum chamber is 0.17 mbar, the laser fluence is kept constant at 1.36 J cm⁻² and the substrate temperature at 700 °C.

IBS^[42] was carried out using a Kaufman source (2.5 cm beam diameter, Ion Tech Inc.) with xenon as sputter gas. Beam current density and the beam voltage were fixed at (4 mA cm⁻²/1000 V) while the partial pressure was <10⁻⁴ mbar and the substrate temperature 700 °C.

For MAD^[43] the precursors were mixed in a suitable molar ratio and dissolved in an organic solvent (DMFA). The substrate was heated resistively by using a SiC heater up to 850 °C and deposition was carried out at ambient air conditions using dried compressed air as spraying gas.

A suitable temperature window was chosen for all techniques to grow fully crystalline (Figure S1f (Supporting Information)) and smooth films (Figure S2 (Supporting Information)). Furthermore, for the PLD and IBS as non-equilibrium techniques the oxygen partial pressure and energy density for photons (see Figure S1a) (Supporting Information)) and ions, respectively, were varied to promote growth in a certain crystal orientation by meeting the correct stoichiometry of the RP-phase (see Figure S1d)). For MAD as a close to equilibrium growth technique the precursor concentrations and solution feeding rates were adjusted for these purposes.

Characterization Methods: X-ray diffraction (XRD, D8 Discovery, Bruker) was employed to analyze the crystallographic structure of targets and thin films. In the setup a Göebel mirror was installed to parallelize the Cu-K α radiation. The corresponding crystal structures were simulated by VESTA.^[44] A scanning electron microscope (SEM, Nova NanoSEM 650, FEI) was used to image the surfaces of targets and thin films. The system is furthermore equipped with a detector for energy dispersive X-ray spectroscopy (EDX, Oxford) to estimate average atomic compositions. With an atomic force microscope (AFM, MFP 3DSA, Asylum Research) the 2D surface morphology was investigated on the sub-nanoscale. Using a focused ion beam machine (Nova Nanolab 600, FEI) thin lamellae were extracted from the thin films for transmission electron microscopy (TEM, Titan 300 keV, Gatan). At the same facility EELS (Quantum ER/965P, Gatan) enables for spatially resolved composition analysis.

Supporting Information

Supporting Information is available from the Wiley Online Library or from the author.

Acknowledgements

The authors would like to thank Bent van Wingerden for his help with electron microscopy and X-ray diffraction, Benjamin Hauschild for PLD, Stephan Melles for IBS and Tobias Meyer and Michael Seibt for helpful discussions. Funding by the Deutsche Forschungsgemeinschaft (DFG) via Grant No. 217133147/SFB1073 projects A02, B02, C01 and Z02 and the use of equipment in the “Collaborative Laboratory and User Facility for Electron Microscopy” (CLUE) www.clue.physik.uni-goettingen.de are gratefully acknowledged.

Open access funding enabled and organized by Projekt DEAL.

Conflict of Interest

The authors declare no conflict of interest.

Data Availability Statement

The data that supports the findings of this study are available in the Supporting Information.

Keywords

epitaxy, Ruddlesden-Popper manganites, thin film growth

Received: November 24, 2020

Revised: January 28, 2021

Published online: February 25, 2021

- [1] C. N. R. Rao, B. Raveau, *Colossal Magnetoresistance, Charge Ordering and Related Properties of Manganese Oxides*, World Scientific, Singapore **1998**.
- [2] A. Asamitsu, Y. Tomioka, H. Kuwahara, Y. Tokura, *Nature* **1997**, *388*, 50.
- [3] W. Westhäuser, S. Schramm, J. Hoffmann, C. Jooss, *Eur. Phys. J. B* **2006**, *53*, 323.
- [4] M. Fiebig, K. Miyano, Y. Tomioka, Y. Tokura, *Science* **1998**, *280*, 1925.
- [5] P. Beaud, A. Caviezel, S. Mariager, L. Rettig, G. Ingold, C. Dornes, S. Huang, J. Johnson, M. Radovic, T. Huber, T. Kubacka, A. Ferrer, H. T. Lemke, M. Chollet, D. Zhu, J. M. Glowina, M. Sikorski, A. Robert, H. Wadati, M. Nakamura, M. Kawasaki, Y. Tokura, S. L. Johnson, U. Staub, *Nat. Mater.* **2014**, *13*, 923.
- [6] B. T. Cong, T. Tsuji, P. X. Thao, P. Q. Thanh, Y. Yamamura, *Phys. B* **2004**, *352*, 18.
- [7] M. Ebrahimzadeh Abrishami, M. Risch, J. Scholz, V. Roddatis, N. Osterthun, C. Jooss, *Materials* **2016**, *9*, 921.
- [8] M. Ibarra, R. Retoux, M. Hervieu, C. Autret, A. Maignan, C. Martin, B. Raveau, *J. Solid State Chem.* **2003**, *170*, 361.
- [9] Y.-H. Chu, M. P. Cruz, C.-H. Yang, L. W. Martin, P.-L. Yang, J.-X. Zhang, K. Lee, P. Yu, L.-Q. Chen, R. Ramesh, *Adv. Mater.* **2007**, *19*, 2662.
- [10] M. Lacotte, A. David, D. Pravarthana, C. Grygiel, G. S. Rohrer, P. A. Salvador, M. Velázquez, R. de Klooe, W. Prellier, *J. Appl. Phys.* **2014**, *116*, 245303.

- [11] S. Majumdar, H. Huhtinen, S. Granroth, P. Paturi, *J. Phys.: Condens. Matter* **2012**, *24*, 206002.
- [12] S. Raabe, D. Mierwaldt, J. Ciston, M. Uijtewaal, H. Stein, J. Hoffmann, Y. Zhu, P. Blöchl, C. Jooss, *Adv. Funct. Mater.* **2012**, *22*, 3378.
- [13] D.-j. Seong, J. Park, N. Lee, M. Hasan, S. Jung, H. Choi, J. Lee, M. Jo, W. Lee, S. Park, S. Kim, Y. H. Jang, Y. Lee, M. Sung, D. Kil, Y. Hwang, S. Chung, S. Hong, J. Roh, H. Hwang, in *2009 IEEE International Electron Devices Meeting (IEDM)*, IEEE, Piscataway, NJ **2009**, pp. 101–104.
- [14] J. Cao, J. Wu, *Mater. Sci. Eng., R* **2011**, *71*, 35.
- [15] A. Herklotz, M. Biegalski, H. Christen, E.-J. Guo, K. Nenkov, A. Rata, L. Schultz, K. Dörr, *Philos. Trans. R. Soc., A* **2014**, *372*, 20120441.
- [16] Z. Huang, K. Han, S. Zeng, M. Motapothula, A. Y. Borisevich, S. Ghosh, W. Lu, C. Li, W. Zhou, Z. Liu, M. Coey, T. Venkatesan, Ariando, *Nano Lett.* **2016**, *16*, 2307.
- [17] R. Zheng, C. Chao, H. L. Chan, C. Choy, H. Luo, *Phys. Rev. B* **2007**, *75*, 024110.
- [18] Z. Yang, Y. Zhang, J. Aarts, M.-Y. Wu, H. Zandbergen, *Appl. Phys. Lett.* **2006**, *88*, 072507.
- [19] K.-T. Wu, Y.-A. Soh, S. J. Skinner, *Mater. Res. Bull.* **2013**, *48*, 3783.
- [20] M. Burriel, G. Garcia, M. D. Rossell, A. Figueras, G. Van Tendeloo, J. Santiso, *Chem. Mater.* **2007**, *19*, 4056.
- [21] K. Shibuya, S. Mi, C.-L. Jia, P. Meuffels, R. Dittmann, *Appl. Phys. Lett.* **2008**, *92*, 241918.
- [22] M. Jungbauer, S. Hühn, R. Egoavil, H. Tan, J. Verbeeck, G. Van Tendeloo, V. Moshnyaga, *Appl. Phys. Lett.* **2014**, *105*, 251603.
- [23] E. Gutmann, A. A. Levin, M. Reibold, J. Müller, P. Paufler, D. C. Meyer, *J. Solid State Chem.* **2006**, *179*, 1864.
- [24] S. Kamba, P. Samoukhina, F. Kadlec, J. Pokorný, J. Petzelt, I. Reaney, P. Wise, *J. Eur. Ceram. Soc.* **2003**, *23*, 2639.
- [25] Y. Takamura, R. V. Chopdekar, J. K. Grepstad, Y. Suzuki, A. F. Marshall, A. Vailionis, H. Zheng, J. F. Mitchell, *J. Appl. Phys.* **2006**, *99*, 08S902.
- [26] R. G. Palgrave, P. Borisov, M. S. Dyer, S. R. McMitchell, G. R. Darling, J. B. Claridge, M. Batuk, H. Tan, H. Tian, J. Verbeeck, J. Hadermann, M. J. Rosseinsky, *J. Am. Chem. Soc.* **2012**, *134*, 7700.
- [27] H. Asano, J. Hayakawa, M. Matsui, *MRS Online Proc. Libr.* **1997**, *494*, 131.
- [28] Q. Lei, M. Golalikhani, B. A. Davidson, G. Liu, D. G. Schlom, Q. Qiao, Y. Zhu, R. U. Chandrasena, W. Yang, A. X. Gray, E. Arenholz, A. K. Farrar, D. A. Tenne, M. Hu, J. Guo, R. K. Singh, X. Xi, *npj Quantum Mater.* **2017**, *2*, 10.
- [29] F. Lyzwa, P. Marsik, V. Roddatis, C. Bernhard, M. Jungbauer, V. Moshnyaga, *J. Phys. D: Appl. Phys.* **2018**, *51*, 125306.
- [30] D. Mierwaldt, V. Roddatis, M. Risch, J. Scholz, J. Geppert, M. E. Abrishami, C. Jooss, *Adv. Sustainable Syst.* **2017**, *1*, 1700109.
- [31] Z. Luo, J. Gao, *J. Appl. Phys.* **2006**, *100*, 056104.
- [32] S. Chi, F. Ye, P. Dai, J. A. Fernandez-Baca, Q. Huang, J. Lynn, E. W. Plummer, R. Mathieu, Y. Kaneko, Y. Tokura, *Proc. Natl. Acad. Sci., U. S. A.* **2007**, *104*, 10796.
- [33] A. J. Ying, C. E. Murray, I. Noyan, *J. Appl. Crystallogr.* **2009**, *42*, 401.
- [34] B. Iffland, J. Hoffmann, T. Kramer, M. Scherff, S. Mildner, C. Jooss, *J. Nanomater.* **2015**, *2015*, 3.
- [35] P. Battle, N. Kasmir, J. Millburn, M. Rosseinsky, R. Patel, L. Spring, J. Vente, S. Blundell, W. Hayes, A. Klehe, A. Mihut, J. Singleton, *J. Appl. Phys.* **1998**, *83*, 6379.
- [36] T. Nakamura, R. Oike, Y. Ling, Y. Tamenori, K. Amezawa, *Phys. Chem. Chem. Phys.* **2016**, *18*, 1564.
- [37] A. Herpers, K. J. OShea, D. A. MacLaren, M. Noyong, B. Rösger, U. Simon, R. Dittmann, *APL Mater.* **2014**, *2*, 106106.
- [38] K. R. Poeppelmeier, M. Leonowicz, J. Scanlon, J. Longo, W. Yelon, *J. Solid State Chem.* **1982**, *45*, 71.
- [39] R. Mathieu, M. Uchida, Y. Kaneko, J. He, X. Yu, R. Kumai, T. Arima, Y. Tomioka, A. Asamitsu, Y. Matsui, Y. Tokura, *Phys. Rev. B* **2006**, *74*, 020404.
- [40] I. Handayani, A. Nugroho, S. Riyadi, G. Blake, N. Mufti, T. Palstra, P. van Loosdrecht, *Phys. Rev. B* **2015**, *92*, 205101.
- [41] H.-U. Krebs, M. Weisheit, J. Faupel, E. Súske, T. Scharf, C. Fuhse, M. Störmer, K. Sturm, M. Seibt, H. Kijewski, D. Nelke, E. Panchenko, M. Buback, in *Advances in Solid State Physics*, Springer, Berlin **2003**, pp. 505–518.
- [42] J. J. Cuomo, S. M. Rossnagel, H. R. Kaufman, *Nucl. Instrum. Methods Phys. Res. B* **1989**, *19–20*, 963
- [43] V. Moshnyaga, I. Khoroshun, A. Sidorenko, P. Petrenko, A. Weidinger, M. Zeitler, B. Rauschenbach, R. Tidecks, K. Samwer, *Appl. Phys. Lett.* **1999**, *74*, 2842.
- [44] K. Momma, F. Izumi, *J. Appl. Crystallogr.* **2008**, *41*, 653.